Materials Transactions, Vol. 64, No. 3 (2023) pp. 650 to 656

Orientation Dependence of Plastic Deformation Behavior and Fracture Energy Absorption Mechanism around Vickers Indentation of Textured Ti_3SiC_2 Sintered Body*[1]

Yuji Shirakami[1,*2], Ken-ichi Ikeda[2,*3], Seiji Miura[2], Koji Morita[3], Tohru S. Suzuki[3] and Yoshio Sakka[3]

[1]*Division of Materials Science and Engineering, Graduate School of Engineering, Hokkaido University, Sapporo 060-8628, Japan*
[2]*Division of Materials Science and Engineering, Faculty of Engineering, Hokkaido University, Sapporo 060-8628, Japan*
[3]*National Institute for Materials Science, Tsukuba 305-0047, Japan*

In order to clarify plastic deformation behavior and mechanism of fracture energy absorption of Ti_3SiC_2, Vickers indentation tests were conducted for Ti_3SiC_2 sintered bodies with various textured orientations. Textured Ti_3SiC_2 sintered bodies were fabricated by slip casting in a strong magnetic field and spark plasma sintering (SPS), and their orientation distribution were analyzed by SEM/EBSD. It was found that for the textured Ti_3SiC_2, the plastic deformation behavior around Vickers indents such as an indent shape and a grain pile-up were strongly affected by basal slip and kink deformation. Furthermore, the fracture energy absorption mechanism around the indents also depended on the texture orientations. From our results, it is concluded that the most effective factor for suppressing the crack propagation was the grain pile-up, and the second one was crack deflections. [doi:10.2320/matertrans.MT-Y2022006]

(Received November 5, 2022; Accepted December 2, 2022; Published December 23, 2022)

Keywords: *Ti_3SiC_2, texture, Vickers indentation, fracture energy absorption, anisotropy*

1. Introduction

Ti_3SiC_2 is a MAX phase ceramic. MAX phase compounds are a class of ternary compounds with more than 70 previously confirmed types that are generally expressed as $M_{n+1}AX_n$. Here, M, A, and X are transition metal elements, group A elements (including group 13 to 16 elements), and C and/or N, respectively. The combination of metals and ceramics exhibits unique properties, resulting from the coexistence of covalent, ionic, and metallic bonding in the crystal structure.[1,2] For instance, similar to ceramics, these compounds are light weight,[1] have a high elastic modulus,[3,4] and exhibit high oxidation[5] and corrosion resistance,[6] while demonstrating thermal[7] and electrical conductivity[8] and thermal shock resistance[9] of metals. Moreover, the crystal structure of Ti_3SiC_2 is hexagonal, and has a layered structure stacked along the *c*-axis. Its lattice constants are $a = 0.3076\,\text{nm}$ and $c = 1.7736\,\text{nm}$. The MAX phases exhibit plastic anisotropy, which is attributed to their high c/a ratio.[10] In Ti_3SiC_2, the basal slip ($\boldsymbol{b} = 1/3\langle 11\bar{2}0\rangle$) is activated preferentially at room temperature, while other slip systems are hardly activated.[11] Owing to the plastic and deformation anisotropy, resulting from the predominant slip system limited in the basal slip, elastic buckling of (0001) results in kink deformation.[12]

There are several reports on the hardness of Ti_3SiC_2 at room temperature. Deformation microstructures have been observed by scanning electron microscope (SEM) or transmission electron microscope (TEM) near indentations, resulting from Vickers hardness or nanoindentation tests.[13–15] Specifically, Molina-Aldareguia *et al.* performed nanoindentation tests on (0001) thin films of Ti_3SiC_2 single crystals, and used TEM observations to confirm the occurrence of delamination and kink deformation around the Berkovich indenter. They modeled the deformation behavior near the indentation by incorporating delamination into the kink deformation mechanism, proposed by Hess *et al.*[16,17] The study revealed that pile-up in single crystals is caused by kink deformation, which would also expect to affect the pile-up in polycrystals. However, there have been no reports of this to date.

Ti_3SiC_2 has a high fracture toughness. To enhance its mechanical properties, Hu *et al.* fabricated textured Ti_3SiC_2 with a unidirectionally aligned *c*-axis by using commercial powder and slip casting in a strong magnetic field and spark plasma sintering (SPS).[18,19] Vickers hardness tests were conducted in directions parallel and perpendicular to the oriented *c*-axis. The tests conducted parallel with the *c*-axis showed that the indentation shape was isotropic, and that cracks occurred in four diagonal directions. In contrast, the tests conducted perpendicular to the *c*-axis showed that the indentation shape became anisotropic, and that the crack propagated only in the basal plane direction. This was attributed to the weak grain boundary and basal plane acting as crack paths. Furthermore, grain push-out was assumed to contribute to crack suppression in the oriented *c*-axis direction.[18] Other MAX phase ceramics showed the same trend.[19–21] These results suggest that the mechanism of fracture energy absorption depends on the crystal orientation; however, the relationship between anisotropic indentation shape and deformation microstructure has not yet been investigated. Therefore, the orientation dependence of plastic deformation behavior and the mechanism of fracture energy absorption near the indentation have not been fully clarified.

This study aims to clarify the effect of orientation on plastic deformation behavior and the mechanism of fracture energy absorption near the indentation in a textured Ti_3SiC_2 sintered body, which was fabricated using slip casting in a magnetic field and SPS.

[*1] This Paper was Originally Published in Japanese in J. Jpn. Soc. Powder Powder Metallurgy **67** (2020) 607–614

[*2] Graduate Student, Hokkaido University. Present address: C&A corporation, Sendai 980-0811, Japan

[*3] Corresponding author, E-mail: ikeda.ken-ichi@eng.hokudai.ac.jp

2. Experimental Procedure

2.1 Preparation of slurry

The slurry was prepared using 30 vol% commercial Ti$_3$SiC$_2$ powder (KANTHAL, Maxthal312) and an ethanol solvent. To effectively apply a magnetic field during slip casting, it was essential to sufficiently disperse the powder in a slurry with high fluidity. To achieve this, 1.5 mass% polyethyleneimine (molecular weight 10,000, FUJIFILM Wako Pure Chemical Corporation) was added to the slurry as a dispersant. The particles were dispersed in the solvent using an ultrasonic homogenizer, while being stirred in a magnetic stirrer at room temperature. The slurry was then defoamed in a vacuum for approximately 10 min to remove any remaining air bubbles.

2.2 Fabrication of textured sintered body

To form the slurry, slip casting was performed using a membrane filter (pore diameter: 0.2 µm) and acrylic cylindrical container (Φ25 mm) in a magnetic field of 12 T using a superconducting magnet (JMTD12T100NC5, JASTEC), while rotating the mold at 30 rpm. The *c*-axis was oriented unidirectionally by applying a magnetic field perpendicular to the casting direction. After molding, green body was sintered by SPS (FUJI-SPS625, Fuji Electronic Industrial Co., Ltd.), which was heated at 600°C for 10 min in a vacuum to remove polyethyleneimine in a carbon die with an inside diameter of 30 mm. After the dispersant was burned out and a high degree of vacuum was confirmed, the atmosphere in the chamber was replaced with Ar. The green body was then sintered at a temperature of 1300°C for 10 min under a uniaxial compressive pressure of 40 MPa. The heating rate was 50°C/min from 600°C to the sintering temperature. Based on density measurements using the Archimedes method, the density of the obtained sintered body was approximately 95% (the theoretical density is 4.52 g/cm^3 1)).

Specimens with three orientations were cut from the sintered body using a high-speed cutting machine and a low-speed diamond cutter. Three indent directions were selected to investigate the orientation dependence of the mechanical properties. The first orientation was parallel to the *c*-axis, the second one was inclined 45° to the former, and the third one was inclined perpendicular to the *c*-axis; hereafter, these orientations are referred to as 0TSC, 45TSC, and 90TSC, respectively. Figure 1 shows a schematic of the specimens with various relationships between the indent direction and *c*-axis.

2.3 Evaluation of textured microstructure

To confirm the microstructure, the top surface of the specimen was mechanically polished with emery paper, diamond slurry, and colloidal silica (particle size: 0.04 µm). Crystal orientation analysis was performed using SEM/electron backscattered diffraction (SEM/EBSD; FE-SEM JSM-6500F, JEOL/OIM Data Collection, TSL Solutions).

2.4 Vickers hardness test

To evaluate the mechanical properties, Vickers tests were performed for 15 s with 2.94, 4.9, 9.8, 27.4, 49, and 98 N loads, and the diagonal length was measured. The deformation microstructure was observed through SEM at loads of 9.8 and 49 N.

3. Results and Discussions

3.1 Evaluation of textured microstructure

Figures 2(a), (c), and (e) show the inverse pole figure (IPF) maps that were measured from the top surfaces of the specimens. Further, Figs. 2(b), (d), and (f) show the corresponding (0001) pole figures (PFs). The grain shape of Ti$_3$SiC$_2$ is presumed to be anisotropic because the grain shape in 0TSC was equiaxed, contrary to the aligned plate-like grains in 90TSC, as shown in Figs. 2(a) and (e), respectively. Moreover, the *c*-axis accumulated at positions of 0°, 45°, and 90° to the loading direction in the results of PFs. Based on these results, the specimens fabricated through slip casting in a strong magnetic field and SPS were appropriate for investigating the orientation dependence of the plastic deformation behavior and the mechanism of fracture energy absorption around the indentation in this study.

3.2 Orientation dependence of Vickers indent shape

Figures 3(a)–(c) present the SEM images of the indents conducted at a load of 9.8 N for each specimen. The indent shape was isotropic in 0TSC, and extended on the right and both sides in 45TSC and 90TSC, respectively. In particular, the results of 0TSC and 90TSC were consistent with the trends reported in the previous research.18) Figure 4 shows the plots of indentation diagonal lengths X and Y at each testing load based on the definition shown in Fig. 3(d). Indentation lengths X and Y in 0TSC did not exhibit significant differences, even as the load increased. However, the difference between X and Y in 45TSC and 90TSC gradually increased, and the difference finally became approximately 50 µm at maximum load. In other words, they exhibited strong anisotropy.

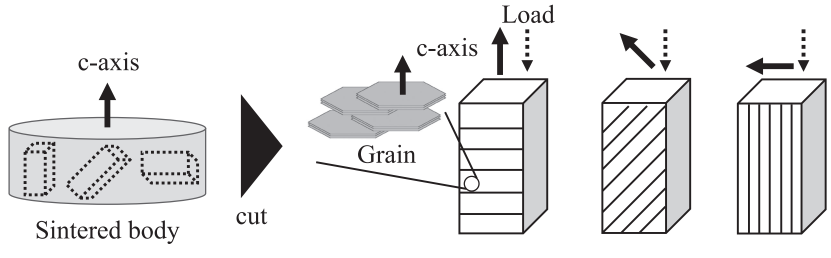

Fig. 1 Schematic illustration of specimens with the various relationship between load direction and *c*-axis.

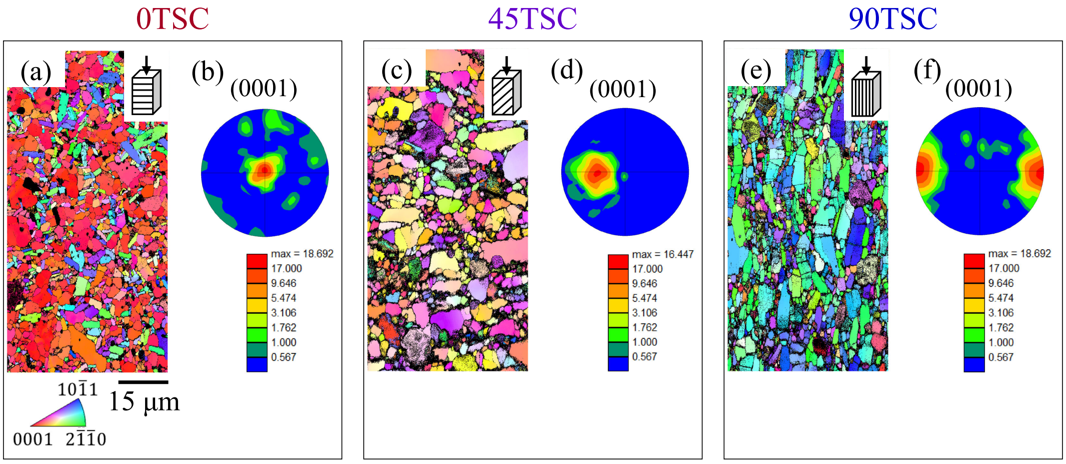

Fig. 2 IPF map and 0001 pole figures on various texture orientation measured from top side.

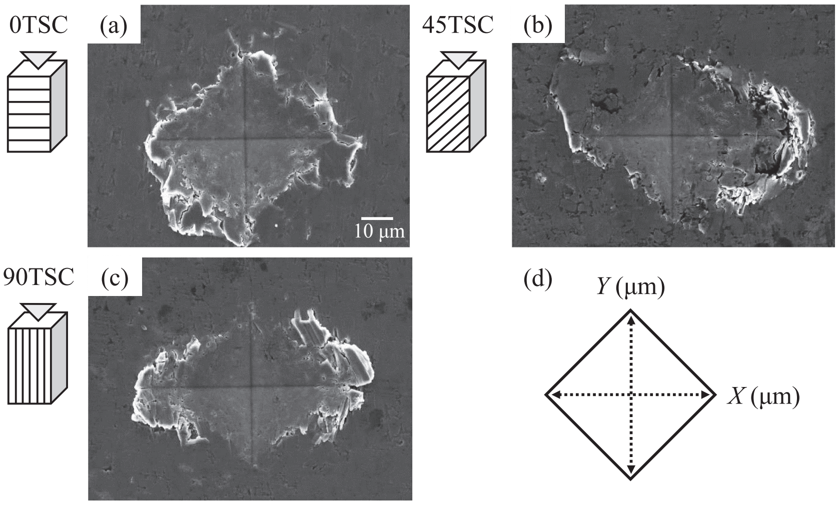

Fig. 3 (a)–(c) SEM images of Vickers indents observed from the top specimens applied 9.8 N, (d) definition of diagonal length direction.

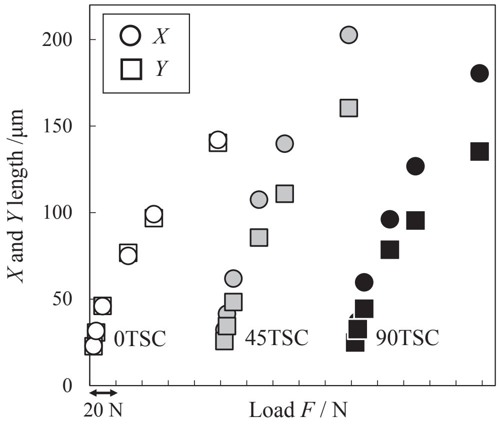

Fig. 4 *X* and *Y* length of the indents on various texture orientation as a function of applied load.

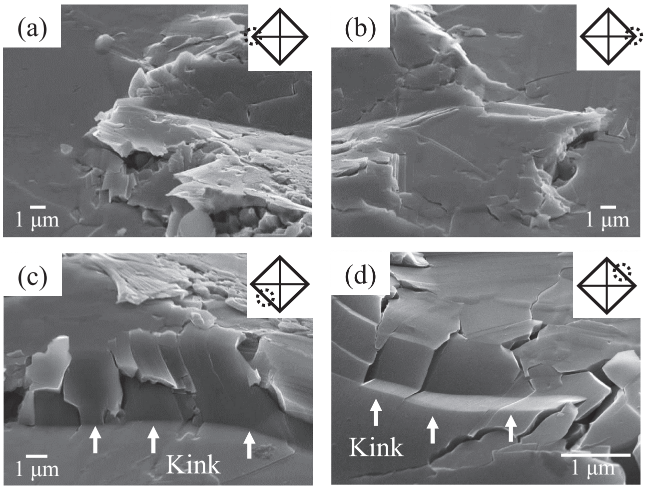

Fig. 5 SEM images tilted 60 deg. of 0TSC.

The direction of the SEM observation was changed from the top surface to oblique 60°, to clarify the plastic deformation around the indentations; the results are shown in Figs. 5–7. Figures 5(a) and 5(b) show tilted images of the indentation on the left and right sides of 0TSC, tested at a load of 9.8 N (corresponding to the position in the inserted schematic). The pile-up occurred because of grain push-out on both sides of the indentation. Furthermore, kink deformation was observed in the magnified images of the lower left and upper right parts of the indents, as shown in Figs. 5(c) and (d). Hence, both grain push-out and kink deformation were associated with the pile-up structure around the indentation.

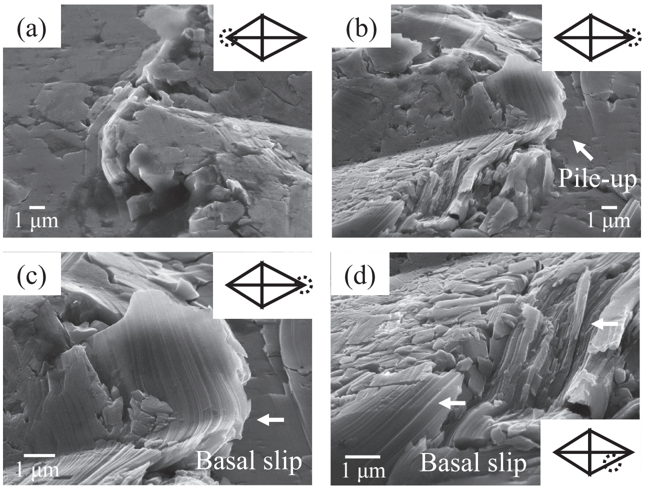

Fig. 6 SEM images tilted 60 deg. of 45TSC.

Figure 6(a) shows the left side of the indentation in 45TSC. Figures 6(b) and (c) show the right side and its enlarged image. The pile-up on the left side is minimal; however, the pile-up on the right side can be clearly observed. A stripe structure on the right side formed by the basal slip was confirmed, remarkably, at the tip of the indentation; thus, the grains were presumed to deform in the shape of the Vickers indenter. Similarly, this characteristic was observed in Fig. 6(d), which shows the lower right side of the indentation.

Figures 7(a) and (b) show both sides of the indentation at 90TSC, and their enlarged images are shown in Figs. 7(c) and (d). Basal slip, delamination, and kink deformation were observed. Higashi *et al.* reported that kink deformation occurs only when a load is applied from a direction perpendicular to the *c*-axis.[22] In other words, basal slip deformation was confirmed for orientations where the compression axis was slightly tilted from the *c*-axis. Slip casting in a strong magnetic field cannot completely control the *c*-axis orientation in polycrystalline materials. Hence, the pile-up in 90TSC was assumed to be caused by the basal slip and kink deformation related to grain constraint.

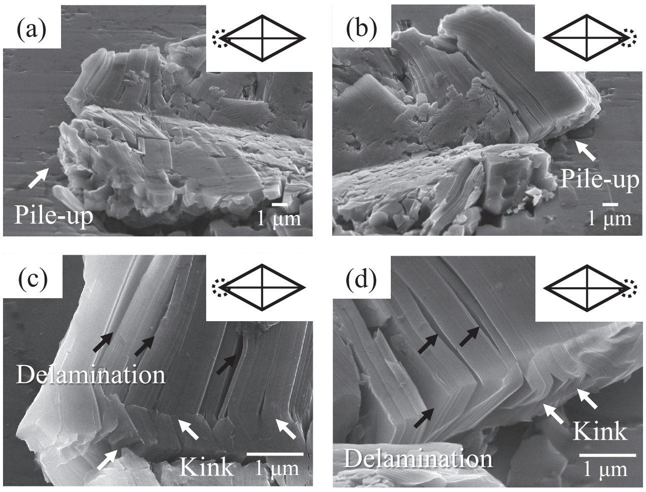

Fig. 7 SEM images tilted 60 deg. of 90TSC.

Figure 8 shows a schematic summarized based on the results in Figs. 5–7. The results do not distinguish how much grain push-out and kink deformation contributed to the pile-up in 0TSC. However, kink deformation occurs, owing to the load from the Vickers indenter that is parallel to the basal plane, following the deformation model proposed by Hess and Barrett.[16] In particular, the magnetic alignment in polycrystalline increases the number of grains loaded parallel to the basal plane, thus increasing the number of kinking grains. The effect of the kink deformation appears to increase with pile-up, which is similar to the result of the (0001) thin film.[17] Moreover, the basal slip in 45TSC and the basal slip and kink deformation in 90TSC were identified as factors contributing to the pile-up.

Figure 9 presents the Vickers hardness that was calculated from the average diagonal length of *X* and *Y*. The Vickers hardness clearly shows the dependence both on the texture orientation and testing load. The Vickers hardness of ceramics is known to exhibit load dependence (i.e., indent size effect (ISE)[23]); thus, it is advisable to test under a wide range of indentation load conditions to identify the load required for steady behavior. Although Hu *et al.* also reported the Vickers hardness of textured Ti_3SiC_2, they evaluated the Vickers hardness of textured Ti_3SiC_2 only using a 9.8 N load.[18] In this study, therefore, the Vickers hardness test was performed in a wide range of load to eliminate ISE.

The hardness of 0TSC, 45TSC, and 90TSC shows higher value at lower loads of <27.4 N and steady behavior of

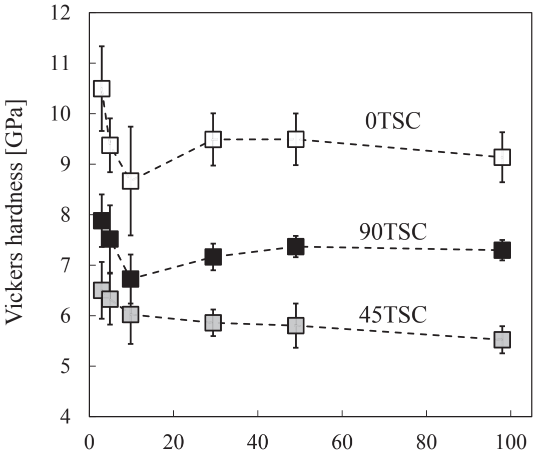

Fig. 9 Vickers hardness on various texture orientation as a function of applied load.

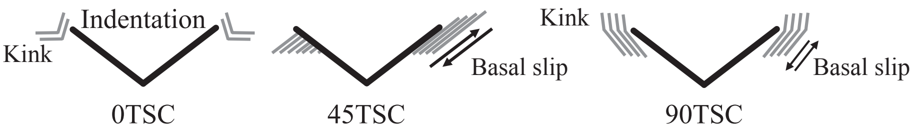

Fig. 8 Summary of plastic deformation around indentation observed from the cross-section.

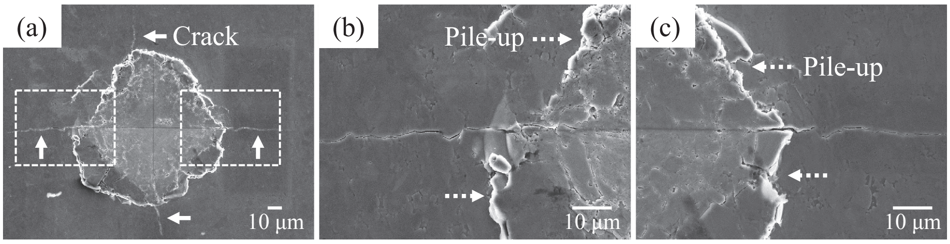

Fig. 10 (a) SEM images of indent in 0TSC applied 49 N, (b) magnified image on left side of indent, (c) magnified image on right side of indent.

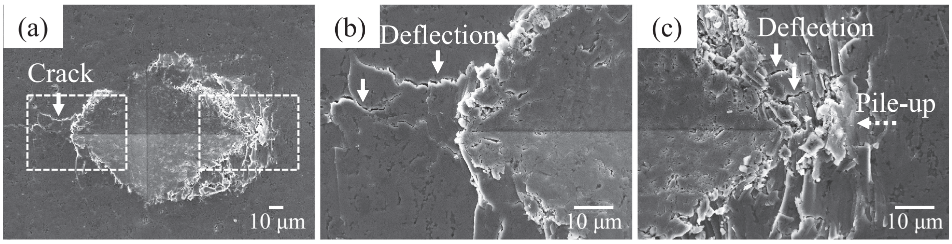

Fig. 11 (a) SEM images of indent in 45TSC applied 49 N, (b) magnified image on left side of indent, (c) magnified image on right side of indent.

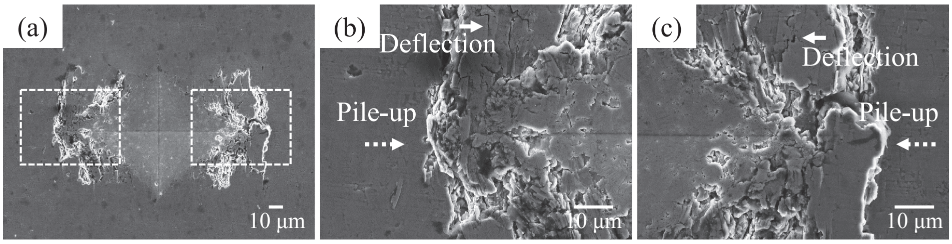

Fig. 12 (a) SEM images of indent in 90TSC applied 49 N, (b) magnified image on left side of indent, (c) magnified image on right side of indent.

approximately 6, 7, and 9 GPa at $\geq$27.4 N, respectively. The hardness of all specimens was 4 GPa higher than that of untextured Ti_3SiC_2.[24] The Vickers hardness test tends to yield incorrect results owing to the anisotropic indent for anisotropic materials.[25] However, this is not the case for the present study. The result of the 0TSC, which shows an isotropic indent shape, indicates that the mechanical properties of Ti_3SiC_2 were drastically improved by controlling the texture via magnetic field alignment.

3.3 Orientation dependence of fracture energy absorption

Figure 10(a) depicts an SEM image of the indent in 0TSC, tested at a load of 49 N. The pile-up and cracks were observed to form in the four diagonal directions around the indent. As shown in Figs. 10(b) and (c), cracks occurred linearly without deflection in the left and right sides of the indent. Although it has generally been reported that the crack deflection by the interlayer and grain boundaries can improve the fracture toughness in Ti_3SiC_2[19] the toughening mechanism did not work in 0TSC due to the texture.

For 45TSC, microstructure around the indent shows anisotropy and morphologies different from those of 0TSC. The cracks were observed only on the left side of the indent, as shown in Fig. 11(a). Contrary to 0TSC, zigzag cracks formed by the deflection were observed on the left side of the indent in Fig. 11(b), and the length of the cracks was much shorter than that in 0TSC. In contrast to the left side, Fig. 11(c) shows that pile-up occurred on the right side because of the basal slip and the crack propagation was highly suppressed due to the crack deflection.

Figure 12(a) shows a typical SEM image of the indent observed in 90TSC. In contrast to 0TSC and 45TSC, no cracks were observed on the right and left sides of the indent. As shown in the enlarged images of Figs. 12(b) and (c), pile-up and crack deflection were confirmed to form on both sides. Accordingly, grain pile-up was a common characteristic for suppressing cracks on the right side of 45TSC and both sides of 90TSC. From these results, pile-up was presumed to be the most effective for realizing effectively fracture energy absorption in textured Ti_3SiC_2.

Thus far, the absorption mechanism has been clarified for 45TSC and 90TSC, but not for 0TSC. In other ceramics (e.g., Al_2O_3), crack propagation is associated with grain size, grain shape, grain boundary character, and cleavage plane orientation.[26,27] As for Ti_3SiC_2, Higashi *et al.* previously reported the cleavage energies in (0001), $\{10\bar{1}0\}$, and $\{11\bar{2}0\}$ using first-principles calculations. According to the calculation results, the cleavage energy of Ti–Si bonding at (0001), which causes delamination, is the lowest. Moreover, it

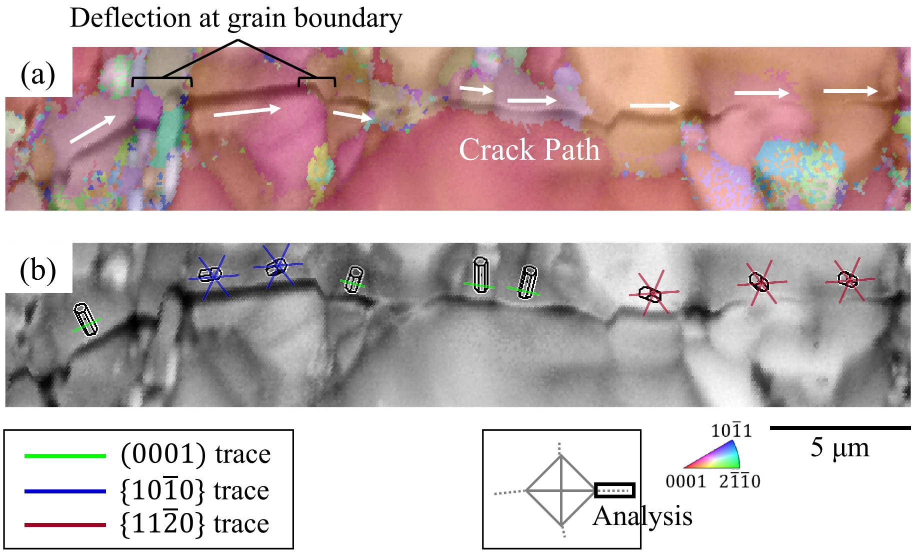

Fig. 13 (a) IQ map superimposed on IPF map around the crack in 0TSC, (b) IQ map with unit cells and various crystal plane traces.

increases in the order of {$11\bar{2}0$} and {$10\bar{1}0$}.[22] This implies that the crack propagates along the crystal plane with lower cleavage energy.

Considering the validity of this hypothesis, the crystal orientation and traces of the crystal plane were analyzed using SEM/EBSD. Figure 13(a) shows the image quality (IQ) map, superimposed over the IPF map near the crack. The cracks passed through the intragranular region, except for two points that deflected at the grain boundaries. Furthermore, they were not completely straight, and micro-scale deflections occurred through the intragranular region. Figure 13(b) shows the IQ map where the traces of (0001), {$10\bar{1}0$}, and {$11\bar{2}0$} are inserted. This figure indicates that the crack propagated along the traces of the major crystal planes in Ti_3SiC_2. Generally, crystal grains are three-dimensional. Similarly, the crack path through the intragranular structure must be examined three dimensionally. This might cause errors in the analysis between the crack path and crystal plane traces. However, these results matched well in the two-dimensional analysis. Hence, the orientation dependence of the crack propagation was suggested, and could be interpreted through the major cleavage plane orientation in Ti_3SiC_2.

4. Conclusion

To clarify plastic deformation behavior and the mechanism of fracture energy absorption of the textured Ti_3SiC_2, Vickers indentation tests were conducted on the specimens with three types of orientations. The key results are summarized as follows.

(1) In a specimen whose *c*-axis is parallel to the load direction, grain pile-up was observed, resulting from kink deformation, as reported for a single-crystal film.
(2) The indentation shape showed noticeable orientation dependence, and basal slip and kink deformation along the Vickers indenter contributed to the anisotropic shape.
(3) The most effective factor for fracture energy absorption was grain pile-up, and the second was crack deflection.
(4) The crack path was suggested to propagate through the major cleavage crystal planes in Ti_3SiC_2.

Acknowledgments

This work was supported by JSPS KAKENHI (Grant Numbers JP19H05115 and JP18H05482) and NIMS Joint Research Hub Program. Parts of this work were also conducted at the Laboratory of Nano-Micro Materials Analysis, Hokkaido University, supported by “Nanotechnology Platform” Program of the Ministry of Education, Culture, Sports, Science and Technology (MEXT), Japan. The authors are grateful to Ms. Nana Hashimoto, a graduate student in the Graduate School of Engineering, Hokkaido University, for her assistance with her contribution to writing the paper.

REFERENCES

1) M.W. Barsoum: Prog. Solid State Chem. **28** (2000) 201–281.
2) C. Hu, H. Zhang, F. Li, Q. Huang and Y. Bao: Int. J. Refract. Met. Hard Mater. **36** (2013) 300–312.
3) R. Pampuch, J. Lis, L. Stobierski and M. Tymkiewicz: J. Eur. Ceram. Soc. **5** (1989) 283–287.
4) P. Finkel, M.W. Barsoum and T. El-Raghy: J. Appl. Phys. **87** (2000) 1701–1703.
5) M.W. Barsoum and T. El-Raghy: J. Electrochem. Soc. **144** (1997) 2508–2516.
6) J. Travaglini, M.W. Barsoum, V. Jovic and T. El-Raghy: Corros. Sci. **45** (2003) 1313–1327.
7) M.W. Barsoum, T. El-Raghy, C.J. Rawn, W.D. Porter, H. Wang, E.A. Payzant and C.R. Hubbard: J. Phys. Chem. Solids **60** (1999) 429–439.
8) M.W. Barsoum, H.-I. Yoo, I.K. Polushina, V.Yu. Rud’, Yu.V. Rud’ and T. El-Raghy: Phys. Rev. B **62** (2000) 10194–10198.
9) M.W. Barsoum and T. El-Raghy: J. Am. Ceram. Soc. **79** (1996) 1953–1956.
10) M.W. Barsoum: Prog. Solid State Chem. **28** (2000) 201–281.
11) L. Farber, M.W. Barsoum, A. Zavaliangos and T. El-Raghy: J. Am. Ceram. Soc. **81** (1998) 1677–1681.
12) M.W. Barsoum, L. Farber and T. El-Raghy: Metall. Mater. Trans. **30** (1999) 1727–1738.
13) T. El-Raghy, A. Zavaliangos, M.W. Barsoum and S. Kalidindi: J. Am. Ceram. Soc. **80** (1997) 513–516.
14) B.J. Kooi, R.J. Poppen, N.J.M. Carvalho, J.Th.M. De Hosson and

M.W. Barsoum: Acta Mater. **51** (2003) 2859–2872.
15) S.B. Li, J.X. Xie, J.Q. Zhao and L.T. Zhang: Mater. Lett. **57** (2002) 119–123.
16) J.B. Hess and C.S. Barrett: Metals Trans. **185** (1949) 599–606.
17) J.M. Molina-Aldareguia, J. Emmerlich, J. Palmquist, U. Jansson and L. Hultman: Scr. Mater. **49** (2003) 155–160.
18) C. Hu, Y. Sakka, S. Grasso, T.S. Suzuki and H. Tanaka: J. Am. Ceram. Soc. **94** (2011) 742–748.
19) Y. Uchida, S. Musha, K. Morita, T.S. Suzuki, T. Nishimura, K. Fujimoto and Y. Sakka: Mater. Trans. **59** (2018) 829–834.
20) C. Hu, Y. Sakka, H. Tanaka, T. Nishimura and S. Grasso: J. Am. Ceram. Soc. **94** (2011) 410–415.
21) Y. Mizuno, K. Sato, M. Mrinalini, T.S. Suzuki and Y. Sakka: J. Ceram. Soc. Jpn. **121** (2013) 366–369.
22) M. Higashi, S. Momono, K. Kishida, N.L. Okamoto and H. Inui: Acta Mater. **161** (2018) 161–170.
23) J. Gong, J. Wu and Z. Guan: J. Eur. Ceram. Soc. **19** (1999) 2625–2631.
24) N.F. Gao and Y. Miyamoto: J. Mater. Sci. **34** (1999) 4385–4392.
25) P.M. Sargent and T.F. Page: J. Mater. Sci. **20** (1985) 2388–2398.
26) M. Iwasa and R.C. Bradt: Adv. Ceram. **10** (1984) 767–779.
27) K. Yasuda, J. Takami, K. Asada, Y. Matsuo and S. Kimura: J. Ceram. Soc. Jpn. **101** (1993) 1384–1389.